



Novel Design of Multi-Layer Cubic Nanoparticles for Achieving Efficient Thin-Film Perovskite Solar Cells

Ali Haghigat¹ · Abbas Ghadimi² · Abdollah Eskandarian¹

Received: 9 April 2024 / Accepted: 6 June 2024 / Published online: 16 June 2024

© The Author(s), under exclusive licence to Springer Science+Business Media, LLC, part of Springer Nature 2024

Abstract

Perovskite solar cells (PSCs) have attracted significant attention due to their promising efficiency and cost-effectiveness. In this study, we first demonstrate the comprehensive optoelectrical analysis of the effect of pure silver (Ag) cubic nanoparticles (NPs) on PSCs with various hole transport layer (HTL) thicknesses and then calculate the optical losses of Ag cubic NPs. Additionally, we propose a novel approach utilizing multi-layer cubic NPs to enhance the power conversion efficiency (PCE) of ultra-thin-film PSCs. The proposed NPs can enhance light absorption and reduce optical losses while providing better stability than pure metallic NPs, which are crucial factors in achieving high-efficiency photovoltaic devices. Thanks to the radiation effects of localized surface plasmon resonance (LSPR), a significant increase in the intensity of far and near fields was shown for the proposed multi-layer cubic NPs, confirming the effectiveness of the proposed NP design. Moreover, PEDOT: PSS performs better than its counterparts in the presence of NPs. In the optimum scenario, the photocurrent exhibits a notable increase of 24.7% compared to the reference cell and a 10.7% increase compared to traditional Ag NPs. Additionally, a PCE of 21.07% was achieved for the absorber material with a thickness of 200 nm. This research opens avenues for developing next-generation PSCs with high performance and NP stability.

Keywords Perovskite solar cells · Hole transport layer · Plasmonic nanoparticles

Introduction

Highlights

- Optimizing the power conversion efficiency of ultra-thin layer perovskite solar cell with pure silver nanoparticles and multi-layer cubic nanoparticles embedded in the perovskite absorber layer.
- The photocurrent for the optimized perovskite solar cell utilizing multi-layer cubic nanoparticles is obtained at 25.60 cm^2 , which is enhanced by approximately 24.78% compared to perovskite solar cells without nanoparticles.
- The proposed solar cell's open-circuit voltage, fill factor, and power conversion efficiency are calculated at around 0.96 V, 85.76, and 21.08%, respectively.
- Based on the results of this study, the proposed configuration of ultra-thin layer perovskite solar cells is suitable for the production of realistic high-performance thin-film perovskite halide solar cells.

✉ Abbas Ghadimi
abbas.ghadimi@iau.ac.ir; aghadimi@gmail.com

¹ Department of Electrical Engineering, Rasht Branch, Islamic Azad University, Rasht, Iran

² Department of Electrical Engineering, Lahijan Branch, Islamic Azad University, Lahijan, Iran

Global warming is a critical issue that could significantly impact human life, making it a top priority for researchers worldwide. Finding alternatives to fossil fuels and embracing green energy solutions is an appealing proposition for researchers in this field. Photovoltaic systems represent the most significant and widely accessible form of green energy. Researchers are optimistic about achieving a total solar energy production of 1 TW by 2030, and the generation of 168 GW of solar energy in 2021 marks a significant step towards realizing this target. Although silicon solar cells hold a prominent position in the market, new solar cell technologies are making remarkable strides toward higher PCE and lower manufacturing costs. PSCs stand out as a hopeful technology that has witnessed remarkable advancements over the course of the last decade [1–3]. In these cells, the perovskite material is sandwiched between an electron-transport layer (ETL) and an HTL. This remarkable growth is attributed to the unique optoelectronic properties of perovskite material, including a high absorption coefficient, a facilitated manufacturing process, tunable bandgap, and low energy bonding [4, 5].

These distinctive properties of perovskite enable the construction of solar cells at sizes significantly smaller than those of their silicon counterparts. The use of thin layers in PSCs is influenced by several factors, including the toxicity associated with lead. The level of lead toxicity is minimized by reducing the perovskite layer (specifically methylammonium). This reduction in thickness also allows for the production of flexible solar cells [6–9]. Reducing the size of the structure presents a challenge of diminished absorption, which is addressed by employing light trapping methods (LT). Various approaches are utilized to LT within the highly compact absorbing material, including techniques such as grating structures [10], plasmonic NPs [11, 12], nanocone arrays [13], and photonic structures [14, 15]. One of the most prevalent approaches in solar cell technology involves the integration of plasmonic NPs. In these solar cells, the absorption characteristics of the absorber material depend on factors like shape, geometry, and the environment around NPs. Modifications to any of these parameters can induce changes in the semiconductor material's absorption properties, directly impacting the solar cell's overall efficiency.

As outlined in previous studies, spherical NPs made of pure metal or metal-dielectric core/shell are commonly used to enhance absorption and PCE [11]. Unlike silicon solar cells, where the integration of metal NPs is straightforward, perovskite-based cells face inherent stability challenges. Consequently, although the integration of pure metal NPs facilitates increased efficiency, it concurrently exacerbates the inherent instability of the device. Moreover, the deployment of pure metal NPs within the absorptive region results in parasitic absorption, necessitating meticulous consideration for its quantification. This, in turn, results in increased manufacturing costs, hindering the commercialization prospects of the final product. Hence, previous studies have utilized Au@TiO_2 core–shell NPs in both spherical and nanorod configurations. The integration of a dielectric shell not only augments absorption but also acts as a protective shield, isolating the NPs from the surrounding absorbing material [16, 17].

Another factor that plays a role in the instability of PSCs is the humidity of the environment. Spiro-OMeTAD (spiro-2,2',7,7'-tetrakis (*N,N*-di-p methoxyphenylamine)9,9'-spirobifluorene) is one of the most common HTLs in PSCs. This material easily transfers the humidity of the environment to the absorber material. Alternative materials like cuprous thiocyanate (CUSCN) and poly(3,4-ethylenedioxythiophene) polystyrene sulfonate (PEDOT: PSS) have exhibited superior stability compared to spiro-OMeTAD [18]. Therefore, in this research article, we propose the integration of advanced dielectric multi-layer cubic NPs to mitigate losses and enhance the stability of NPs without compromising the stability of PSC. These NPs aim to achieve higher performance than traditional pure

metal NPs. Additionally, we systematically investigate three commonly used HTLs, i.e., spiro-OMeTAD, CUSCN, and PEDOT: PSS in PSCs to assess their optical responses and determine the optimal performance when coupled with the proposed multi-layer cubic NPs.

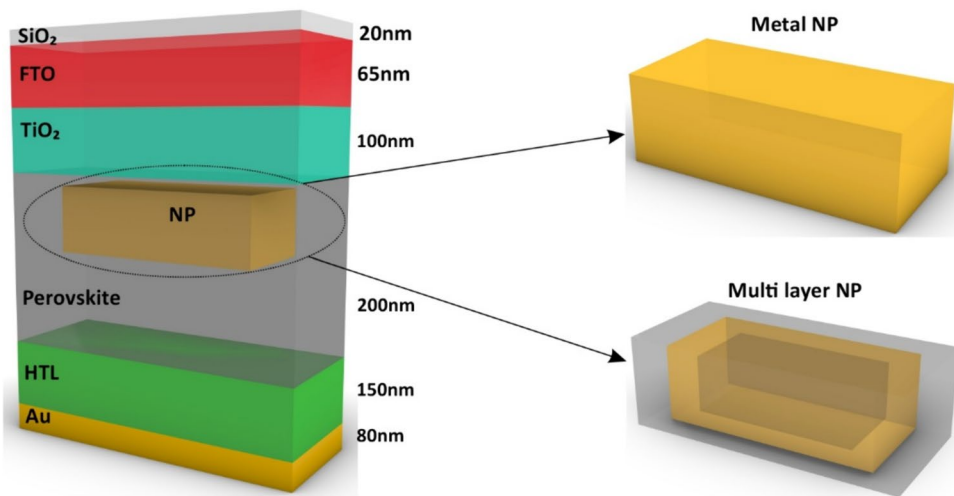
This study's initial focus is examining the optical response of ultra-thin-film PSCs with three commonly employed HTLs. Following this analysis, we introduce pure Ag cubic NPs into the ultra-thin-film PSCs configuration to augment light absorption and evaluate their associated optical losses. Subsequently, we explore the integration of multi-layer cubic NPs as replacements for their metallic counterparts. This strategic substitution aims to minimize light losses to the greatest extent feasible while concurrently bolstering the stability of the NP, thereby contributing to overall device robustness. Furthermore, the utilization of these NPs serves a dual purpose by mitigating optical losses and maximizing light absorption as an additional source of photon carriers. Through meticulous optimization, we demonstrate that incorporating the proposed NPs, particularly when combined with the PEDOT: PSS layer, yields the most favorable optical response, thus presenting a promising pathway toward enhancing the efficiency and stability of ultra-thin-film PSCs.

Device Structure and Simulation

At the outset of this research study, we present a three-dimensional schematic of an ultra-thin-film PSC in Fig. 1. The solar cell configuration comprises several layers to optimize device performance and protect against environmental pollutants. Firstly, a 20-nm-thick silica (SiO_2) is a protective barrier for the device. Following this, a transparent conductive oxide (TCO) layer composed of fluorine-containing tin oxide (FTO), also 65 nm in thickness, is employed due to its superior stability and enhanced charge transfer capabilities compared to alternatives such as indium-doped tin oxide (ITO) or aluminum-doped zinc oxide (AZO) [19, 20]. Subsequently, a 100-nm-thick titanium oxide (TiO_2) layer functions as the ETL, facilitating electron extraction and hole blocking. The ultra-thin absorber layer of perovskite (MAPbI_3), 200 nm thick, is positioned beneath the electron transfer layer, serving as the primary absorber of incident light. The subsequent layer is HTL, with a thickness of 150 nm, utilizing commonly employed materials denoted as spiro-OMeTAD, CUSCN, and PEDOT: PSS. These materials are widely utilized in PSCs to facilitate efficient hole transport. Finally, the outermost layer consists of an 80-nm-thick gold metal contact, facilitating efficient charge extraction from the device.

Inherently, the MAPbI_3 absorber material exhibits high absorption at initial wavelengths, primarily attributed to its

Fig. 1 Three-dimensional schematic of ultra-thin-film PSC with proposed multi-layer cubic NPs



extinction coefficient. However, absorption tends to decrease at longer wavelengths. Photon management emerges as a practical solution to enhance absorption, particularly for wavelengths exceeding 600 nm. Plasmonic NPs leverage the well-known phenomenon of LSPR and the resultant amplification of electromagnetic fields surrounding them to effectively manage photons and achieve maximal light harvesting for the absorber material. Enhancing the efficiency of solar cells using metal NPs involves both far-field and near-field radiation effects. Nonradiative effects such as hot electron transfer (HET) and plasmon resonant energy transfer (PRET) also contribute to this improvement. When sunlight enters the absorber with high albedo, it scatters into the far field after interacting with the metal NPs. The scattering cross-section can be significantly larger than the physical cross-section of the metal NPs. The emitted light is then reabsorbed by the absorber material at distances of several hundred nanometers, further increasing the total light trapped in the solar cells, a phenomenon known as far-field scattering.

On the other hand, near-field enhancement occurs when the interaction between photons and free electrons in metals leads to plasmonic resonance. This interaction forms powerful electromagnetic fields around the NPs, significantly higher than the incident light, which can focus light at nanometer scales. Thus, metal NPs act as secondary light sources, increasing light absorption and photon flux. In both radiation effects, the intensity of the field strongly depends on factors such as the morphology, location, and materials of plasmonic NPs. The surrounding environment of the NPs also plays a crucial role. The first non-radiative effect observed in plasmonic NPs is a quantum mechanical phenomenon known as Landau damping. This phenomenon, typically studied over timescales of 1–100 femtoseconds using spectroscopy, occurs when a plasmon undergoes non-radiative decay, generating hot electron–hole pairs during the relaxation process due to the anisotropy of the LSPR. In

core–shell NPs, for HET to facilitate absorption, the dielectric layer must be thinner than the electron tunneling barrier. Conversely, the PRET effect is not limited by the electron tunneling barrier. The PRET effect is similar to Förster resonant energy transfer (FRET), a well-known phenomenon in fluorescent systems where energy transfers from an excited donor molecule to an acceptor molecule via dipole–dipole coupling. In PRET, the fluorescent molecule is replaced by the LSPR dipole of plasmonic NPs, arising from the collective oscillations of conduction electrons within the NPs. When photons interact with metallic NPs, the LSPR dipole experiences dephasing due to plasmon decoherence caused by absorption or scattering processes. After light absorption, PRET occurs when resonant energy transfers from the metal NPs to an adjacent semiconductor material via dipole–dipole coupling, generating excitons within the semiconductor either below or near the band edge. In PRET, the plasmonic NPs act as a mediator, facilitating energy transfer from the metal to the semiconductor. It is important to note that the dominant effect in plasmonic solar cells is attributed to radiation effects [11, 21]. Therefore, only radiation effects are considered in this study.

Consequently, previous studies have explored the incorporation of these NPs within solar cells, embedded within electron transport layer (ETL) and HTL materials, as well as within the absorber material itself. However, for optimal utilization of plasmonic NPs and their effects, it is advisable to incorporate them directly into the absorber medium. While numerous theoretical and experimental investigations have been conducted on solar cells in previous generations, integrating NPs into absorber materials like perovskite presents a novel challenge. In addition to the inherent instability of perovskite, these materials possess corrosive properties that can compromise the integrity of NPs over time, especially upon contact with metal surfaces. Hence, using a protective shield becomes imperative to safeguard NPs, chosen for their stability. Dielectric materials

typically serve this purpose due to their inherent stability and non-reactive nature. Furthermore, the common utilization of the spiro-OMeTAD/Au interface in PSC structures, this configuration has been associated with the instability of perovskite [22, 23]. In pursuit of enhanced stability, alternative materials for the HTL, such as CUSCN and PEDOT: PSS, have garnered attention. Furthermore, it's notable that the optical response of various HTL materials to NPs within the absorber layer exhibits distinct characteristics.

In our investigation, we have selected the three-dimensional finite-difference time-domain (3D-FDTD) technique for the optical modeling of optical devices. By utilizing 3D-FDTD, we solve Maxwell's equations to derive the intensity of the electric field, typically represented as $|E(r, \lambda)|$. Following this, we compute the absorption spectrum range for the ultra-thin-film PSC utilizing Eq. (1) while considering the cut-off of the absorbing material.

$$A(r, \omega) = \frac{1}{2} \frac{\omega \epsilon_0 \text{Im}(\epsilon(r, \omega)) |E(r, \omega)|^2}{P_{in}} \quad (1)$$

Here, P_{in} represents the standard lighting condition with a power of 1000 W/m². The symbols ω and r denote specific locations and angular frequency, respectively. The dielectric constant of the medium is represented by ϵ , while the electrical permittivity of the vacuum is denoted by ϵ_0 . Equation (1) is utilized to compute the optical losses of NPs. Net absorption is obtained by subtracting optical losses from total absorption, as depicted in Eq. (2).

$$A_{\text{net}}(\lambda) = \int_{V_{\text{absorber}}} A(r, \lambda) dV - \int_{V_{\text{nano particles}}} A(r, \lambda) dV \quad (2)$$

According to Eq. (3), we utilize the integral over the absorption range of perovskite to determine the numerical value of photocurrent.

$$J_{SC} = \int_{300nm}^{800nm} A(\lambda) \cdot AMI \cdot 5D(\lambda) d\lambda \quad (3)$$

Equation (4) shows the electron–hole generation rate values.

$$G(x, y, z, \lambda) = \frac{\epsilon_0}{2\hbar} \frac{\text{Im}(\epsilon(r, \lambda)) |E(r, \lambda)|^2}{P_{in}} \quad (4)$$

Additionally, the number of electron–hole pairs generated at each point is shown by Eq. (5). This equation quantifies the generation of charge carriers within the absorber material as a result of light absorption, providing essential information about the photovoltaic response of the device.

$$G(x, y, z, \lambda) = \int G(x, y, z, \lambda) d\lambda \quad (5)$$

After completing the optical analysis, we transition to the electrical analysis. In Eq. (6), E , ϵ_S , ρ , and ψ , represent the electric field, static material permittivity, space charge density, and electrostatic potential, respectively. Moreover, q , N_D , and N_A denote the elementary charge, ionized donor density, and acceptor density, respectively. These symbols are instrumental in characterizing the electrical behavior of the PSC, facilitating the understanding of charge transport and carrier dynamics within the device.

$$\frac{\partial^2 \psi}{\partial^2 x} = -\frac{\partial E}{\partial x} = -\frac{\rho}{\epsilon_S} = \frac{q}{\epsilon_S} [p - n + N_D(x) - N_A(x) \pm N_{def}(x)] \quad (6)$$

Additionally, Eq. (7) represents the carrier continuity equation for electrons, while Eq. (8) depicts the carrier continuity equation for holes.

$$\frac{\partial J_n}{\partial x} + G - U_n(n, p) = 0 \quad (7)$$

$$-\frac{\partial J_p}{\partial x} + G - U_p(n, p) = 0 \quad (8)$$

Here, G represents the electron–hole pair generation rate. J_n and J_p denote the electron and hole carrier current densities, respectively. U_p and U_n represent the net recombination rates for holes and electrons, respectively. These parameters play key roles in characterizing the charge carrier recombination within the PSC, influencing its overall PCE.

$$J_n = qp\mu_n E + qD_n \frac{\partial n}{\partial x} \quad (9)$$

$$J_p = qp\mu_p E + qD_p \frac{\partial p}{\partial x} \quad (10)$$

The physical equations governing the device end with the well-known diffusion equations (Eqs. 9 and 10). In these equations, μ_n and D_n represent the mobility and diffusion coefficients of the electron carrier, respectively. Similarly, μ_p and D_p represent the mobility and diffusion coefficients of the hole carrier, respectively. Additionally, q denotes the elementary charge, serving as the primary charge symbol. These equations play a pivotal role in modeling the transport of charge carriers within the PSC, incorporating both drift under an electric field and diffusion due to concentration gradients [11, 22, 23].

Results and Discussion

In the initial phase, our analysis focuses on examining the light absorption characteristics of the device. Maximizing light harvesting is crucial for enhancing the PCE of the device; therefore, extensive research efforts have been dedicated to studying the photocurrent within the solar cell. The optical analysis was conducted using the finite difference time domain (FDTD) simulation method, renowned for its efficiency in modeling light propagation in complex structures. Given the critical role of boundary conditions in FDTD analysis, meticulous consideration was given to their selection. Perfectly matched layer (PML) boundary conditions were employed to efficiently absorb outgoing waves in the direction of sunlight, ensuring an accurate representation of light absorption. Additionally, periodic boundary conditions (PBC) were implemented in the X and Y directions to simulate an infinitely repetitive structure. To ensure high accuracy in the simulation, the smallest mesh size of 1 nm has been utilized in the direction of the radiation of the plane wave source. Additionally, it is worth noting that the length of the period in the X and Y

directions is set at 200 nm. The refractive indices of the materials utilized in the simulation are sourced from previous studies, ensuring the reliability and accuracy of our analysis [11, 24–30].

In the first step, we consider the reference structure depicted in Fig. 1. At this stage, we consider three cases of PSCs; in all three cases, we embedded Ag cubic NPs in the photoactive region. The difference between the three cases is in the HTL layer, where case 1 uses PEDOT: PSS material for HTL, and cases 2 and 3 PSC use spiro-OMeTAD and CUSCN materials as HTL layers, respectively. The cube surfaces are systematically varied in the range of 50 to 100 nm, and the resulting changes in photocurrent are illustrated in the diagram in Fig. 2a. Notably, it is observed that for cases 2 and 3, the optimal choice is a pure Ag cube NP with a size of 80 nm, while for case 1, a size of 70 nm is preferred. Furthermore, Fig. 2b compares the photocurrent levels with and without NPs to highlight the enhanced performance achieved in the optimal case.

Figure 2b depicts that case 2 exhibits the lowest photocurrent without NPs, recorded at a value of 19.29 mA/cm^2 . Following the embedding of NPs in the photoactive region,

Fig. 2 **a** Photocurrent response as a function of thicknesses of cubic Ag NP within a PSC, for cases 1–3. **b** Photocurrent bar chart for cases 1–3 (without (W/O) NP and with (W) cubic NP). **c** PSC absorption in the presence of best-case cubic NP for cases 1–3. **d** Diagram of optical losses of NP and net absorption for case 1

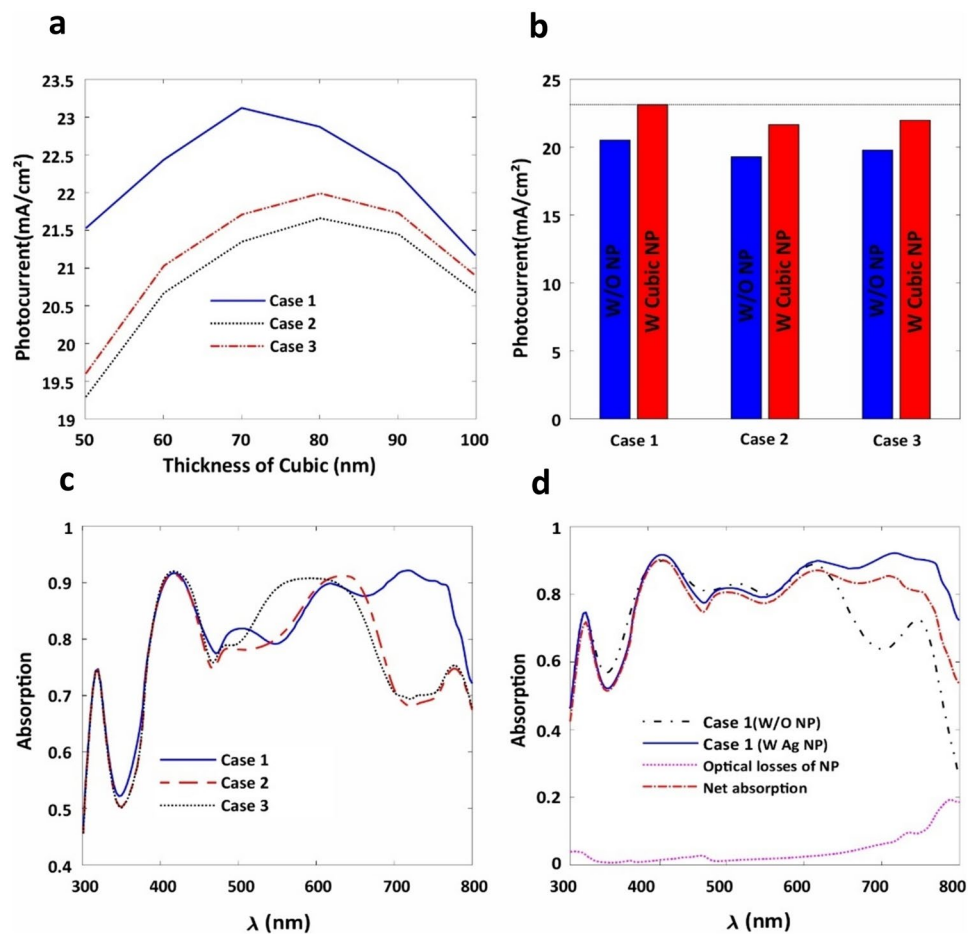
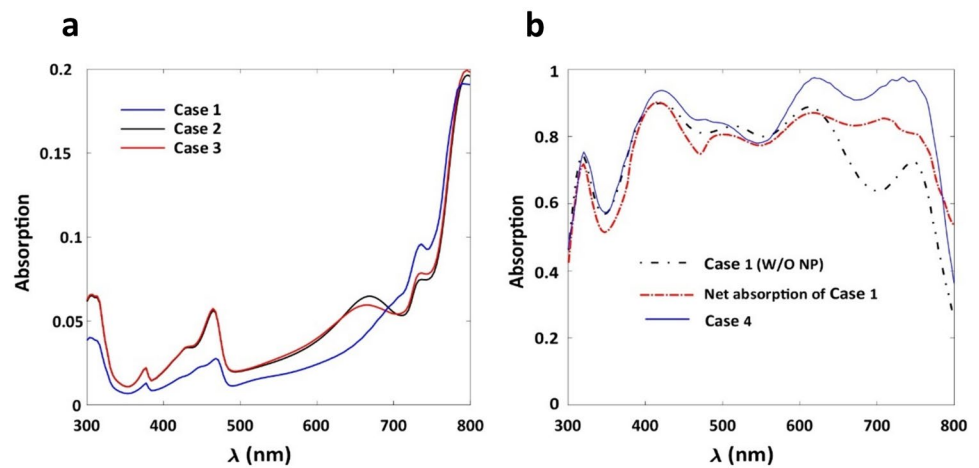


Fig. 3 **a** Optical losses of optimized Ag NPs for cases 1–3. **b** Absorption diagram comparing case 1 (without (W/O) NP, net absorption with Ag NP) and absorption with case 4



this photocurrent rose to 21.66 mA/cm^2 , marking a notable increase of 12.3%. Similarly, case 3 initially displayed a photocurrent of 19.79 mA/cm^2 without NPs, which rose to approximately 22 mA/cm^2 after their addition, reflecting an increase of 11.2%. Finally, case 1 demonstrated an initial photocurrent of 20.52 mA/cm^2 without NPs, which increased by 12.8% to approximately 23.13 mA/cm^2 following the NP incorporation. We analyze the difference in absorption across the spectrum in the presence of optimal NPs.

As illustrated in the absorption diagram, from wavelengths ranging between 300 and 480 nm, all three materials exhibit the same performance, including pure Ag cubic NP. However, within the wavelength range of 500 to 600 nm, case 2 demonstrates superior absorption, while in the range of 620 to 800 nm, case 1 surpasses the others. In other words, this diagram confirms the photocurrent value of the previous step. As previously discussed, optical loss is a significant challenge associated with metal NPs utilized in the photoactive region. Consequently, for

the optimal photocurrent case (i.e., case 1), we meticulously computed the optical loss of NP and utilized this information to calculate the net absorption, as depicted in Fig. 2d. It is imperative to note that larger NPs result in increased optical loss. As mentioned, the optimal size of NPs for cases 2 and 3 is 80 nm, resulting in higher losses than the optimal case (see Fig. 3a). Furthermore, as discussed in previous experimental studies, CuSCN and PEDOT: PSS exhibited lower hysteresis curves and better stability than spiro-OMeTAD [31, 32]. Furthermore, it is well known that the refractive index significantly influences optical analysis. CuSCN and PEDOT: PSS exhibit similar curves, while spiro-OMeTAD behaves differently [11, 30, 33].

To minimize optical losses, we propose the use of multi-layered NPs. These NPs comprise a thin middle layer of metal sandwiched between two dielectric layers, effectively replacing pure silver NPs. Leveraging the exceptional properties of silica, such as high chemical and thermal stability, we utilized it as the dielectric material. The use

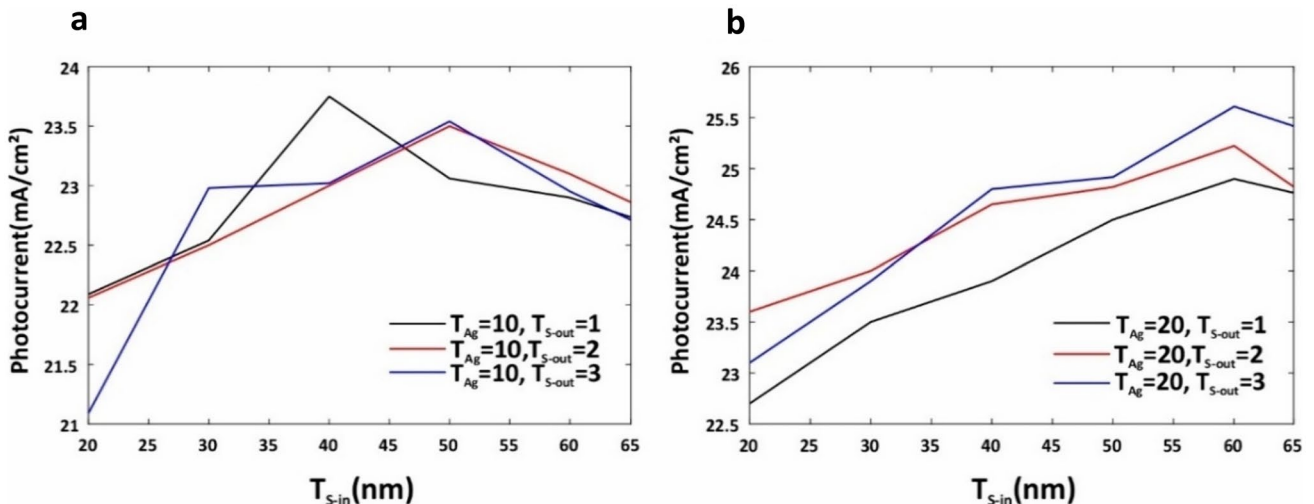


Fig. 4 **a** Photocurrent as a function of $T_{S\text{-in}}$ when T_{Ag} is 10 nm and $T_{S\text{-out}}$ ranges from 1 to 3 nm. **b** Photocurrent as a function of the $T_{S\text{-in}}$ when T_{Ag} is 20 nm and $T_{S\text{-out}}$ ranges from 1 to 3 nm

of multi-layered NPs in PSCs offers two significant advantages. First, the dielectric shell protects against the corrosive properties of the perovskite (methylammonium) material and prevents the recombination of excitons on the metal surface [34, 35]. Second, because the metal is sandwiched between two dielectric layers and is very small, it avoids parasitic absorption and can prevent thermal and chemical interactions, thereby improving the stability of the device [16, 35–39]. Therefore, we introduce case 4, a PSC with PEDOT: PSS material and multi-layered NPs placed in the photoactive area. Figure 4 displays a portion of the sweeps. In Fig. 4a, the changes in the inner SiO_2 thickness ($T_{\text{S-in}}$) are

shown in terms of photocurrent when the Ag thickness (T_{Ag}) is 10 nm and the outer SiO_2 thickness ($T_{\text{S-out}}$) ranges from 1 to 3 nm. In Fig. 4b, the changes in the $T_{\text{S-in}}$ are illustrated in terms of photocurrent when the T_{Ag} is 20 nm and the $T_{\text{S-out}}$ ranges from 1 to 3 nm.

As shown in Fig. 4, after optimizing the size parameters for the dielectric core, we selected 60 nm for the Ag middle layer, 20 nm for the inner dielectric shell, and 3 nm for the outer dielectric shell. Consequently, the photocurrent reached 25.60 mA/cm^2 , representing a 10.7% and 24.78% increase compared to pure Ag NPs and without NPs, respectively. Figure 3 depicts the absorption diagram of the

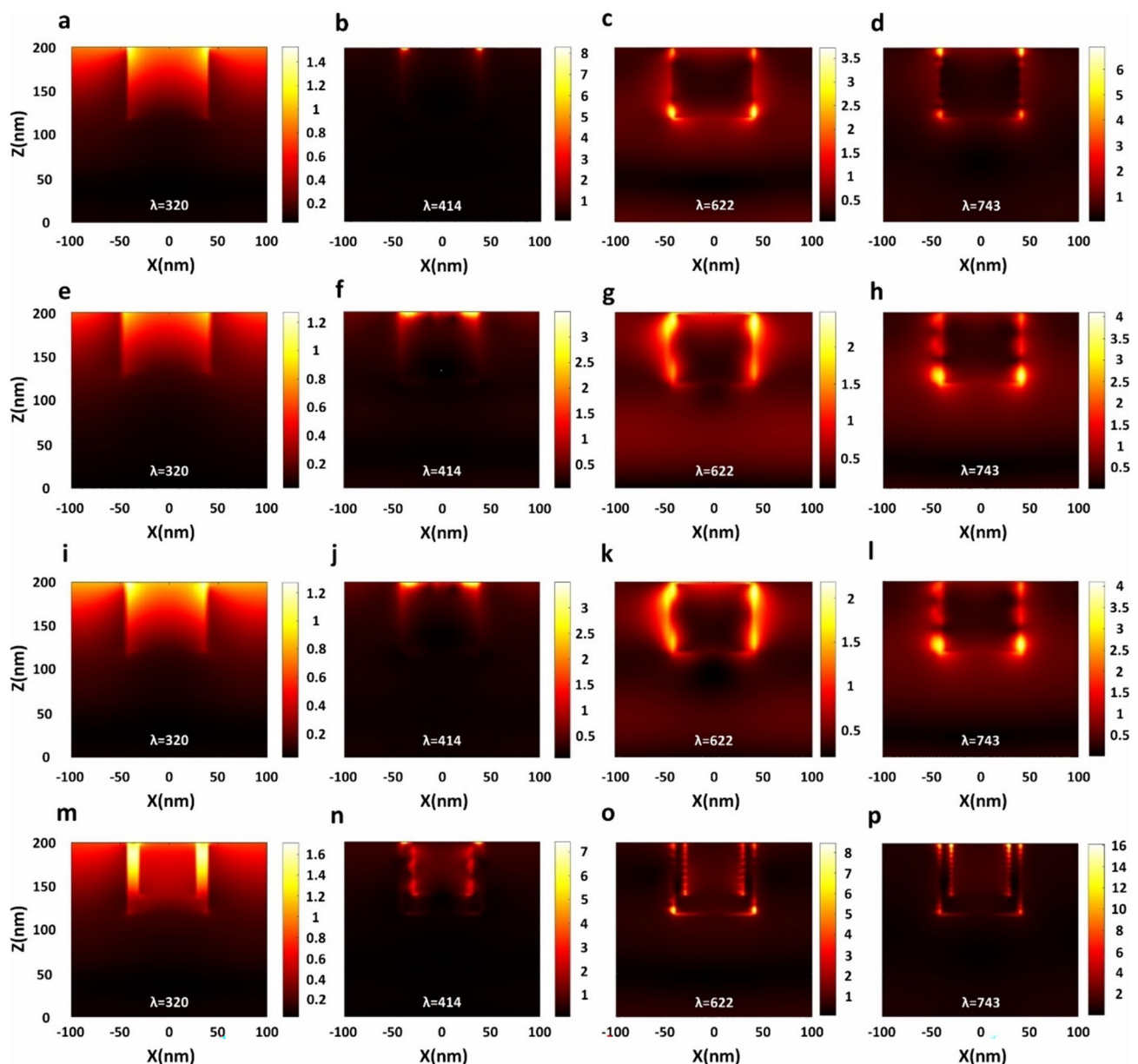
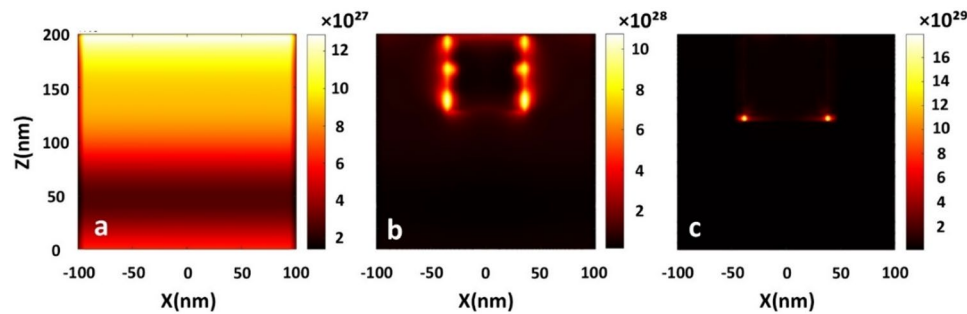


Fig. 5 Distribution of electromagnetic fields of cases 1–4 at the following wavelengths: **a, e, i, m** 320 nm, **b, f, j, n** 414 nm, **c, g, k, o** 622 nm, and **d, h, l, p** 743 nm

Fig. 6 Generation rate for the ultra-thin-film PSC under the following conditions: **a** without NPs, **b** with pure Ag NPs, and **c** with proposed multi-layer cubic NPs



proposed multi-layer cubic NPs compared to the state without NPs and pure Ag NPs. The proposed multi-layer cubic NPs exhibit over 85% absorption for wavelengths beyond 600 nm, surpassing the absorption capabilities of cells without NPs, which experience a loss of absorption in this range. As indicated in previous studies, the distribution of electromagnetic fields around proposed multi-layer cubic NPs significantly influences the enhancement of photocurrent [11, 22, 23]. Therefore, we investigate the electromagnetic field distribution at different wavelengths. Figure 5a–d of case 1, Fig. 5e–h for case 2, Fig. 5i–l for case 3, and Fig. 5m–p indicate the distribution of electromagnetic fields for case 4.

For all cases, at a wavelength of 320 nm, no discernible effect of the field distribution is observed, indicating minimal interaction between light and cubic NPs. Consequently, as depicted in the absorption diagrams, no increase in absorption attributable to the cubic NPs is feasible at this wavelength. However, at a wavelength of 414 nm, effects related to far fields emerge, known as the antenna effect. As depicted in Fig. 5o, p, in the wavelengths of 622 and 743 nm, a notably strong electromagnetic field is observed around the proposed multi-layer cubic NPs (both near and far fields), facilitating photon absorption as a secondary light source [21, 40]. As can be seen in the photo, the intensity of these fields for the proposed NP at wavelengths 622 and 743 nm is higher than that of Ag cubic NPs (cases 1–3). It shows the unique performance of proposed multi-layer cubic NPs in

wavelengths where perovskite has a loss of absorption. Consequently, as demonstrated earlier in the absorption diagram, absorption is increased at these wavelengths.

The generation rate of electron and hole pairs in the photoactive region is a critical factor influencing the final PCE of the ultra-thin-film PSC. In the subsequent step, we examine the generation rate of electron and hole pairs in the PSC for cases 1 and 4. As depicted in Fig. 6a. Naturally, the minimal electron–hole pair generation rate is associated with the absence of NPs within the photoactive region. The highest electron–hole pair generation rate is attributed to the proposed multi-layer cubic NPs, representing an increase compared to pure Ag NPs (see Fig. 6b, c). In essence, the proposed multi-layer cubic NPs minimize charge carrier recombination, resulting in prolonged carrier lifetimes and an enhancement in overall efficiency. Furthermore, the proposed multi-layer cubic NPs facilitate efficient charge transfer within the perovskite layer.

Following the optical analysis's conclusion, we conduct the solar cell's electrical analysis to meticulously examine essential parameters, including open-circuit voltage (V_{oc}), fill factor (FF), and PCE. All the indispensable parameters required for the electrical simulation have been documented in Table 1, meticulously curated from previous works [23, 41–44]. Moreover, the carrier generation rate assumes a crucial role as a primary input in the solar cell capacitance simulator (SCAPS) software [22, 45].

Table 1 Electrical modeling input parameters

Parameter	FTO	TiO ₂	MAPbI ₃	PEDOT:PSS	Au [23]
Work function (eV)	–	–	–	–	5.1 [23]
Band gap (eV)	3.2 [22, 23]	3.1 [22, 23]	1.5 [41]	1.6 [44]	–
Electron affinity (eV)	4.2 [22, 23]	4.1 [22, 23]	3.93 [41]	3.4 [44]	–
Dielectric permittivity (relative)	9 [22, 23]	10 [22, 23]	24.1 [42]	3 [44]	–
CB effective density of states (cm⁻³)	1×10^{19} [22, 23]	1×10^{19} [22, 23]	8.1×10^{18} [42]	2.2×10^{18} [44]	–
VB effective density of states (cm⁻³)	1×10^{19} [22, 23]	1×10^{19} [22, 23]	8.1×10^{18} [42]	1.8×10^{19} [44]	–
Electron mobility (cm² V⁻¹ s⁻¹)	20 [22, 23]	0.02 [22, 23]	1 [22, 23]	0.045 [44]	–
Hole mobility (cm² V⁻¹ s⁻¹)	10 [22, 23]	0.02 [22, 23]	20 [22, 23]	0.045 [44]	–
Doping concentration of donors (ND; cm⁻³)	1×10^{22} [22, 23]	1×10^{16} [41]	$1 \times 10^{+9}$ [23]	–	–
Doping concentration of acceptors (NA; cm⁻³)	–	–	$1 \times 10^{+9}$ [23]	$1 \times 10^{+15}$ [44]	–

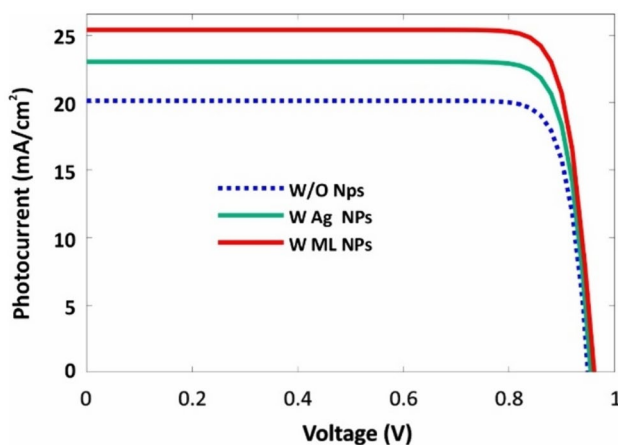


Fig. 7 J-V characteristics for the ultra-thin-film PSC under the following conditions: without NPs, with pure Ag NPs, and with proposed multi-layer cubic NPs

Figure 7 illustrates the J-V characteristics for the ultra-thin-film PSC in the reference state, with traditional Ag NPs (case 1) and proposed multi-layer cubic NPs (case 4). As anticipated, the maximum benefit is observed with the proposed multi-layer cubic NPs. All outputs from this section are summarized in Table 2. In the optimum scenario, the photocurrent exhibits a notable increase of 24.7% compared to the reference cell and a 10.7% increase compared to traditional Ag NPs.

The optimum case of this study shows a 20.3% improvement in efficiency compared to recent similar studies on perovskite solar cells with Au/TiO₂ core–shell nanorods in the photoactive region [17]. Additionally, our results indicate a 24.3% improvement in efficiency compared to models that simultaneously use photonic structures and plasmonic NPs [14]. In Table 3, the output parameters of this study and those involved in similar studies are listed.

Table 2 Optimized PSC output parameters for the reference cell, with pure Ag NPs, and with proposed multi-layer cubic NPs

PSC structure	Type of NPs	JSC (mA/cm ²)	FF	V _{oc} (V)	η (%)
Cases 1 and 4	W/O NPs	20.52	86.06	0.95	16.78
Case 1	W Ag NPs	23.13	85.72	0.96	19.03
Case 4	W ML NPs	25.60	85.76	0.96	21.08

Table 3 The output parameters of this study and other PSCs

PSC	JSC (mA/cm ²)	FF	V _{oc} (V)	η (%)
This work (case 4)	25.60	0.857	0.96	21.08
This work (case 1)	23.13	0.857	0.96	19.03
PSC [11]	22.28	0.88	1.003	19.71
PSC [46]	23.85	0.757	1.06	18.28
PSC [17]	21.80	0.832	0.96	17.51
PSC [14]	22.26	0.824	0.923	16.94
PSC [47]	19.74	0.774	1.098	16.78
PSC [48]	20.56	0.782	1.09	16.77
PSC [49]	20.31	0.847	0.94	16.20
PSC [50]	21.5	0.67	1.07	15.4

Conclusion

This work presents a comprehensive coupled optoelectrical study on a PSC featuring three different HTL materials. The study reveals that, optically, the PEDOT: PSS HTL material performs optimally in the presence of traditional cubic Ag NPs. However, due to the optical losses associated with traditional cubic Ag NPs, we replaced them with dielectric/metal/dielectric (SiO₂/Ag/SiO₂) cubic NPs. This substitution improved field effects around the proposed multi-layer cubic NPs and enhanced generation rates, as evidenced by our optical analysis. Moreover, the thermal and chemical stability of the proposed model is expected to surpass that of its traditional counterpart. For the optimal model, the photocurrent exhibited a significant increase of 24.7% compared to the reference cell and a 10.7% increase compared to traditional Ag NPs. The best-case numerical values also showed a J_{SC} of 25.60 mA/cm², a V_{OC} of 0.96 V, an FF of 0.857, and a PCE of 21.08%. Our research underscores the potential for commercializing the proposed multi-layer cubic NPs based on their performance, representing a significant advancement in high-efficiency ultra-thin-film PSCs.

Author Contributions Ali Haghighe designed the model and the computational framework and analyzed the data. Ali Haghighe and A. Ghadimi carried out the implementation. Ali Haghighe and A. Ghadimi performed the calculations. Ali Haghighe and A. Ghadimi wrote the manuscript with input from all the authors. Ali Haghighe, A. Ghadimi, and A. Eskandarian conceived the study and were in charge of overall direction and planning.

Data Availability No datasets were generated or analyzed during the current study.

Declarations

Competing Interests The authors declare no competing interests.

References

- Alkhalayfeh MA, Aziz AA, Pakhuruddin MZ, Katubi KMM (2021) Recent advances of perovskite solar cells embedded with plasmonic nanoparticles. *Physica Status Solidi (a)* 218:2100310
- Green MA, Ho-Baillie A, Snaith HJ (2014) The emergence of perovskite solar cells. *Nat Photonics* 8:506–514
- Jangjoy A, Bahador H, Heidarzadeh H (2019) Design of an ultra-thin silicon solar cell using localized surface plasmonic effects of embedded paired nanoparticles. *Opt Commun* 450:216–221
- Stranks SD, Snaith HJ (2015) Metal-halide perovskites for photovoltaic and light-emitting devices. *Nat Nanotechnol* 10:391–402
- Sun S, Salim T, Mathews N, Duchamp M, Boothroyd C, Xing G, Sum TC, Lam YM (2014) The origin of high efficiency in low-temperature solution-processable bilayer organometal halide hybrid solar cells. *Energy Environ Sci* 7:399–407
- Zhang Y, Park N-G (2020) A thin film (< 200 nm) perovskite solar cell with 18% efficiency. *J Mater Chem A* 8:17420–17428
- Schileo G, Grancini G (2021) Lead or no lead? Availability, toxicity, sustainability and environmental impact of lead-free perovskite solar cells. *J Mater Chem C* 9:67–76
- Talebi H, Emami F (2023) High performance ultra-thin perovskite solar cell by surface plasmon polaritons and waveguide modes. *Opt Laser Technol* 165:109552
- Ullah S, Ullah S, Wang J, Yang S-E, Xia T, Guo H, Chen Y (2020) Investigation of air-stable Cs₂SnI₆ films prepared by the modified two-step process for lead-free perovskite solar cells. *Semicond Sci Technol* 35:125027
- Deng K, Liu Z, Wang M, Li L (2019) Nanoimprinted grating-embedded perovskite solar cells with improved light management. *Adv Func Mater* 29:1900830
- Jangjoy A, Matloub S (2022) Optical simulation and design of high-absorption thin-film perovskite halide solar cells based on embedded quadrilateral cluster nanoparticles. *Sol Energy* 242:10–19
- Ullah H, Khan AD, Ullah A, Ullah I, Noman M (2016) Plasmonic perfect absorber for solar cell applications. In: 2016 International Conference on Emerging Technologies (ICET) IEEE 1–5
- Tai M, Zhao X, Shen H, Guo Y, Zhang M, Zhou Y, Li X, Yao Z, Yin X, Han J (2019) Ultrathin Zn₂SnO₄ (ZTO) passivated ZnO nanocone arrays for efficient and stable perovskite solar cells. *Chem Eng J* 361:60–66
- Ullah I, Guo J, Wang C, Liu Z, Li X, Jiang L, Yuan J, Ma W (2023) Design and analysis of high-efficiency perovskite solar cell using the controllable photonic structure and plasmonic nanoparticles. *J Alloy Compd* 960:170994
- Ullah I, Ullah MI, Ma W, Yuan J (2024) Nanotextured highly efficient optical and light trapping strategies using efficient hole transport-free structure for perovskite solar cells. *Opt Commun* 556:130276
- Ullah I, Saghaei H, Khan J, Shah SK (2022) The role of plasmonic metal-oxides core-shell nanoparticles on the optical absorption of perovskite solar cells. *Opt Quant Electron* 54:675
- Ullah I, Hossain MA, Armghan A, Rana MS, Al Asad MA (2023) The optoelectronic enhancement in perovskite solar cells using plasmonic metal-dielectric core-shell and nanorod nanoparticles. *Opt Quantum Electron* 55:1018
- Dijk G, Rutz AL, Malliaras GG (2020) Stability of PEDOT: PSS-coated gold electrodes in cell culture conditions. *Adv Mater Technol* 5:1900662
- Wei Q, Yang Z, Yang D, Zi W, Ren X, Liu Y, Liu X, Feng J, Liu SF (2016) The effect of transparent conductive oxide on the performance CH₃NH₃PbI₃ perovskite solar cell without electron/hole selective layers. *Sol Energy* 135:654–661
- Latif H, Liu J, Mo D, Wang R, Zeng J, Zhai P, Sattar A (2021) Effect of target morphology on morphological, optical and electrical properties of FTO thin film deposited by pulsed laser deposition for MAPbBr₃ perovskite solar cell. *Surf Interfaces* 24:101117
- Erwin WR, Zarick HF, Talbert EM, Bardhan R (2016) Light trapping in mesoporous solar cells with plasmonic nanostructures. *Energy Environ Sci* 9:1577–1601
- Jangjoy A, Matloub S (2024) Optimizing carbon-based perovskite solar cells with pyramidal core–shell nanoparticles for high efficiency. *Plasmonics* 1–11
- Jangjoy A, Matloub S (2023) Theoretical study of Ag and Au triple core–shell spherical plasmonic nanoparticles in ultra-thin film perovskite solar cells. *Opt Express* 31:19102–19115
- Hajjiah A, Kandas I, Shehata N (2018) Efficiency enhancement of perovskite solar cells with plasmonic nanoparticles: a simulation study. *Materials* 11:1626
- van Eerden M, Jaysankar M, Hadipour A, Merckx T, Schermer JJ, Aernouts T, Poortmans J, Paetzold UW (2017) Optical analysis of planar multicrystalline perovskite solar cells. *Adv Opt Mater* 5:1700151
- Palik ED (1998) *Handbook of optical constants of solids* (Academic Press) 3
- Leguy AM, Hu Y, Campoy-Quiles M, Alonso MI, Weber OJ, Azarhoosh P, Van Schilfgaarde M, Weller MT, Bein T, Nelson J (2015) Reversible hydration of CH₃NH₃PbI₃ in films, single crystals, and solar cells. *Chem Mater* 27:3397–3407
- Zhukovsky SV, Andryieuski A, Takayama O, Shkondin E, Malureanu R, Jensen F, Lavrinenko AV (2015) Experimental demonstration of effective medium approximation breakdown in deeply subwavelength all-dielectric multilayers. *Phys Rev Lett* 115:177402
- Larraquert JI, Rodríguez-de Marcos L, Méndez JA, Martín P, Bendavid A (2013) High reflectance ta-C coatings in the extreme ultraviolet. *Opt Express* 21:27537–27549
- Chen C-W, Hsiao S-Y, Chen C-Y, Kang H-W, Huang Z-Y, Lin H-W (2015) Optical properties of organometal halide perovskite thin films and general device structure design rules for perovskite single and tandem solar cells. *J Mater Chem A* 3:9152–9159
- Yang Y, Hoang MT, Yao D, Pham ND, Tiong VT, Wang X, Wang H (2020) Spiro-OMeTAD or CuSCN as a preferable hole transport material for carbon-based planar perovskite solar cells. *J Mater Chem A* 8:12723–12734
- Kim H-S, Jang I-H, Ahn N, Choi M, Guerrero A, Bisquert J, Park N-G (2015) Control of I-V hysteresis in CH₃NH₃PbI₃ perovskite solar cell. *J Phys Chem Lett* 6:4633–4639
- Pattanasattayavong P, Ndjawa GON, Zhao K, Chou KW, Yaacob-Gross N, O'Regan BC, Amassian A, Anthopoulos TD (2013) Electric field-induced hole transport in copper (I) thiocyanate (CuSCN) thin-films processed from solution at room temperature. *Chem Commun* 49:4154–4156
- He Z, Zhang C, Meng R, Luo X, Chen M, Lu H, Yang Y (2020) Influence of Ag@ SiO₂ with different shell thickness on photoelectric properties of hole-conductor-free perovskite solar cells. *Nanomaterials* 10:2364
- Wang Y, Zhai J, Song Y, He L (2016) The Ag shell thickness effect of Au@ Ag@ SiO₂ core–shell nanoparticles on the

- optoelectronic performance of dye sensitized solar cells. *Chem Commun* 52:2390–2393
- 36. Dang X, Qi J, Klug MT, Chen P-Y, Yun DS, Fang NX, Hammond PT, Belcher AM (2013) Tunable localized surface plasmon-enabled broadband light-harvesting enhancement for high-efficiency panchromatic dye-sensitized solar cells. *Nano Lett* 13:637–642
 - 37. Baek S-W, Noh J, Lee C-H, Kim B, Seo M-K, Lee J-Y (2013) Plasmonic forward scattering effect in organic solar cells: a powerful optical engineering method. *Sci Rep* 3:1726
 - 38. Jankovic V, Yang Y, You J, Dou L, Liu Y, Cheung P, Chang JP, Yang Y (2013) Active layer-incorporated, spectrally tuned Au/SiO₂ core/shell nanorod-based light trapping for organic photovoltaics. *ACS Nano* 7:3815–3822
 - 39. Wu R, Yang B, Zhang C, Huang Y, Cui Y, Liu P, Zhou C, Hao Y, Gao Y, Yang J (2016) Prominent efficiency enhancement in perovskite solar cells employing silica-coated gold nanorods. *J Phys Chem C* 120:6996–7004
 - 40. Erwin WR, Coppola A, Zarick HF, Arora P, Miller KJ, Bardhan R (2014) Plasmon enhanced water splitting mediated by hybrid bimetallic Au–Ag core–shell nanostructures. *Nanoscale* 6:12626–12634
 - 41. Yadav P, Pandey K, Bhatt P, Raval D, Tripathi B, Pandey MK, Kumar M (2015) Exploring the performance limiting parameters of perovskite solar cell through experimental analysis and device simulation. *Sol Energy* 122:773–782
 - 42. Sherkar TS, Momblona C, Gil-Escríg L, Bolink HJ, Koster LJA (2017) Improving perovskite solar cells: insights from a validated device model. *Adv Energy Mater* 7:1602432
 - 43. Alipour H, Ghadimi A (2021) Optimization of lead-free perovskite solar cells in normal-structure with WO₃ and water-free PEDOT: PSS composite for hole transport layer by SCAPS-1D simulation. *Opt Mater* 120:111432
 - 44. Hossain MK, Toki GI, Kuddus A, Rubel M, Hossain M, Bencherif H, Rahman MF, Islam MR, Mushtaq M (2023) An extensive study on multiple ETL and HTL layers to design and simulation of high-performance lead-free CsSnCl₃-based perovskite solar cells. *Sci Rep* 13:2521
 - 45. Burgelman M, Nollet P, Degrave S (2000) Modelling polycrystalline semiconductor solar cells. *Thin Solid Films* 361:527–532
 - 46. Fu N, Bao ZY, Zhang Y-L, Zhang G, Ke S, Lin P, Dai J, Huang H, Lei DY (2017) Panchromatic thin perovskite solar cells with broadband plasmonic absorption enhancement and efficient light scattering management by Au@ Ag core-shell nanocuboids. *Nano Energy* 41:654–664
 - 47. Ma C, Liu C, Huang J, Ma Y, Liu Z, Li L-J, Anthopoulos TD, Han Y, Fratalocchi A, Wu T (2019) Plasmonic-enhanced light harvesting and perovskite solar cell performance using Au biometric dimers with broadband structural darkness. *Solar RRL* 3:1900138
 - 48. Irandoost R, Soleimani-Amiri S (2020) Design and analysis of high efficiency perovskite solar cell with ZnO nanorods and plasmonic nanoparticles. *Optik* 202:163598
 - 49. hosein Mohammadi M, Eskandari M, Fathi D (2021) Effects of the location and size of plasmonic nanoparticles (Ag and Au) in improving the optical absorption and efficiency of perovskite solar cells. *J Alloys Compd* 877:160177
 - 50. Liu M, Johnston MB, Snaith HJ (2013) Efficient planar heterojunction perovskite solar cells by vapour deposition. *Nature* 501:395–398

Publisher's Note Springer Nature remains neutral with regard to jurisdictional claims in published maps and institutional affiliations.

Springer Nature or its licensor (e.g. a society or other partner) holds exclusive rights to this article under a publishing agreement with the author(s) or other rightsholder(s); author self-archiving of the accepted manuscript version of this article is solely governed by the terms of such publishing agreement and applicable law.